Received: 4 May 2022 | Revised: 29 November 2022 | Accepted: 25 January 2023

DOI: 10.1002/mawe.202200088

ARTICLE

WILEY VCH

Finite element based model for predicting induced residual stresses and cutting forces in AISI 1020 steel alloy

Finite Elemente basiertes Modell zur Abschätzung von induzierten Eigenspannungen und Schnittkräften in einer AISI 1020 (S 275 JR) Stahllegierung

R. N. Bosire | O. M. Muvengei | J. M. Mutua | J. K. Kimotho

Department of Mechanical Engineering, Jomo Kenyatta University of Agriculture and Technology, Juja, Kenya

Correspondence
R. N. Bosire, Department of Mechanical Engineering, Jomo Kenyatta University of Agriculture and Technology, Juja, Kenya.
Email: info.rodgerbos@gmail.com

Abstract

The application of finite element models is a promising method for ensuring part quality during machining to accurately predict induced residual stresses and cutting forces. The present study applied Analysis System software to formulate a 3D model to predict induced residual stress and forces for AISI 1020 alloy. Taguchi method was applied in the design of the experiment with three levels and three factors selected: Cutting speed, feed rate and depth of cut. For validation, stresses are measured using an x-ray diffractometer from the surface to a depth of 0.6 mm in steps of 0.2 mm. The cutting forces are determined using a force dynamometer. Simulation results showed that cutting speed, feed rate and depth of cut contributed 94.76 %, 0.048 %, and 0.11 % respectively. The predictive model equations were statistically significant with a p-value of < 0.005. The average induced residual stress on the superficial layer from the experiment and simulation were −367.7 MPa and −365.6 MPa respectively. The average residual stresses obtained at depths of 0.2 mm, 0.4 mm, and 0.6 mm were −260 MPa, −233 MPa, and −211 MPa, respectively. The proposed model offers a potential solution to reducing the costs of experimental methods.

KEYWORDS
3D model, experiment, induced residual stress, simulation, Taguchi

SCHLÜSSELWÖRTER
3D Modell, Experiment, induzierte Eigenspannung, Simulation, Taguchi

1 | INTRODUCTION

Studying residual stress induction during machining helps in addressing the quality of machined products by ensuring they have dimensional stability, toughness and strength to prevent failure when subjected to cyclic loads. Residual stresses are the internal multiaxial static stress distribution locked into a material without the application of external force. The heterogeneous plastic deformation in a component generates induced residual stresses during turning, milling, and shaping operations [1, 2]. The combined thermal effects and chip formation

process leads to the formation of residual stresses in cylindrical components [3].

Orthogonal machining is the turning operation used in producing circular components, majorly from steel alloys. During the orthogonal cutting process, the tool pressure on the workpiece produces plastic deformation that results in the generation of residual stresses on and subsurface layers of the workpiece [4–6].

The conventional methods of measuring induced residual stress are expensive and time-consuming. To solve the challenges, researchers embarked on applying finite element models to design models for predicting residual stresses and cutting forces. The input design variables are selected for optimization and tool specifications for effective modelling [7, 8].

Researchers have used numerical simulations for studying various structural and flow phenomena in steel alloys [9]. A finite element-based model is vital in predicting resultant forces, induced residual stresses, wear and tear of a tool and temperature variation during the machining processes. Besides machining, simulation researchers have extensively used finite element simulation [10, 11].

A mathematical simulation approach was proposed to study the mechanics orthogonal cutting process. The focus was to understand the formation of a continuous type of chips and the modelling of cutting forces. The deformation zone theory developed showed the equilibrium of chip formation using the maximum energy principle and heat partition contribution on residual stresses during the orthogonal cutting process [12–14].

The simulation approach was applied in the hard turning of high carbon AISI D2 steel alloy and the results obtained demonstrated that the microstructure alterations, induced residual stresses, and surface roughness affect the surface integrity. It was discovered that the behavior of the residual stresses correlates to the input parameters and the sensitivity of the induced residual stress depends on the input parameters [15].

Finite element modelling was applied to analyze the effect of the uncoated tool insert. The two-dimensional model was developed by Abaqus software and validated by experimental investigation. The results showed that the crater wears increased with increasing feed rate [16].

The occurrence of non-uniform machining forces during the turning operation of aluminium and steel alloys forms a significant challenge [17]. While modelling residual stress for 4340 steel, it was demonstrated that machining forces and temperature variation contribute mainly to the formation of induced residual stresses and tool wear [18]. While investigating the effect of process parameters on residual stresses in orthogonal cutting of AISI 1045 alloy, it was discovered that speed and cutting depth contribute significantly to the induction of residual stresses [19].

Simulation and modelling by finite element analysis and commercial software like Ansys, Abaqus, and Advantedge have become alternative routes in studying the influence of cutting parameters on cutting forces and induced residual stresses [20]. Despite many attempts to address the challenges in measuring forces and residual stresses, limited data is available on verifying and validating 3D finite element models developed for carbon steels.

2 | PRESENT FINITE ELEMENT MODELLING USING ANSYS SOFTWARE

Steel machining is a complex mechanical process, hence for effective finite element simulation, reliable flow stresses, frictional, chip and thermal models need to be applied. The mechanical and thermal properties of the work material AISI 1020 alloy are presented, Tables 1, 2.

TABLE 1 Mechanical properties of work material for modelling AISI 1020 alloy [6].

Density $\rho[kg/m^3]$	Young's modulus, E [GPa]	Poisson's ratio, n	Ultimate strength, σ_u [MPa]	Yield strength, σ_y [MPa]
7870	200	0.29	420	350

TABLE 2 Thermal and mechanical properties of high-speed steel T1 [21].

Density ρ $[kg/m^3]$	Young's modulus, E [Gpa]	Poisson's ratio, n	Thermal expansion ε [μm/m °C]	Rockwell hardness HRC	Specific heat capacity, $[J\,kg^{-1}K^{-1}]$
8670	210	0.1	9.7×10^{-6}	63	460

2.1 | Mechanical modelling equations

The motions for a two-dimensional orthogonal cutting operation are stated, Equations 1, 2 [22]:

$$\frac{\partial \sigma_{xx}}{\partial x}+\frac{\partial \sigma_{xy}}{\partial y}+\rho b_x=\rho\frac{\partial^2 U}{\partial t^2} \tag{1}$$

$$\frac{\partial \sigma_{xx}}{\partial x}+\frac{\partial \sigma_{xy}}{\partial y}+\rho b_x=\rho\frac{\partial^2 U}{\partial t^2} \tag{2}$$

where: x-y is the reference coordinate system, σ Cauchy stress, ρ density, b body force, t, and U are time and material displacement, respectively. A general form is obtained when finite element discretization and weak formulation are used, Equation 3 [22].

$$[M]\{\ddot{U}\}+\{R_{int}\}=\{R_{ext}\} \tag{3}$$

where: $[M]$ is the mass, $\{\ddot{U}\}$ acceleration vector, $\{R_{int}\}$ is the internal force vector and $\{R_{ext}\}$ is the external force vector. In this case, the effect of damping is not considered, hence $\{\mathrm{R_{int}}\}$ can be formulated, Equation 4.

$$\{R_{int}\}=[C_d]\{\dot{U}\}+[K_s]\{U\}=[K_s]\{U\},\ [C_d]\cong 0 \tag{4}$$

where: $[C_d]$ is the damping stiffness matrix and $[K_s]$ is the stiffness matrix. $\{R_{ext}\}$ involves the support's reaction forces during the cutting operation and external forces applied.

2.2 | Thermal modelling

Heat transfer occurs from primary, secondary, and tertiary deformation zones during the orthogonal cutting operation. The equation governing the heat transfer for the finite element is presented, Equation 5.

$$\rho c\left(\frac{\partial T}{\partial t}+V_x\frac{\partial T}{\partial x}+V_y\frac{\partial T}{\partial y}\right)=k\left(\frac{\partial^2 T}{\partial x^2}+\frac{\partial^2 T}{\partial y^2}\right)+\dot{Q}_g \tag{5}$$

where: T is the temperature, c specific heat capacity, k is the thermal conductivity. $\dot{Q}_g$ is the total heat generated from primary and secondary deformation.

Based on Equation 5, the total heat generated can be calculated, Equation 6 [22–26].

$$\dot{Q}_g=\eta_p W_p+\dot{\eta_F W_F}=\eta_p(\sigma\dot{\varepsilon_p})+\eta_F(\tau V_{Ch}) \tag{6}$$

where: η_p is the inelastic heat fraction (Taylor-Quinney coefficient), η_F is the fraction of friction work converted to heat. $\dot{W}_p$ is the rate of plastic work per unit material volume while $\dot{W}_F$ is the rate of frictional work per unit contact area. σ is the flow stress. $\dot{\varepsilon_p}$ is the effective plastic strain. Also, τ and V_{Ch} are frictional shear stress at the tool-chip interface and chip velocity along with the tool-chip interface.

2.3 | Work material modelling

The work material for the simulation is AISI 1020 Steel alloy shaft with 50 mm diameter and 100 mm length. This is low-carbon steel commonly used in designing cylindrical shafts, pipes, crankshafts, and couplings. The Johnson-Cook model equation is adopted in modelling the workpiece because it provides a good fit for strain-hardening behavior, and it is numerically robust, Equation 7.

$$\bar{\sigma}=\left[A+B\bar{\varepsilon}^{\ n}\right]\left[1+Cln\frac{\dot{\varepsilon}}{\varepsilon_o}\right]\left[1-\left(\frac{T-T_r}{T_m-T_r}\right)^m\right] \tag{7}$$

where: A is the yield stress of the material under reference conditions, B is the strain hardening constant, n is the strain hardening coefficient, C is the strengthening coefficient of strain rate, m is the thermal softening coefficient, T_m is melting temperature, T_r is room temperature, $\varepsilon_\circ$ is the shear strain, $\bar{\sigma}$ the extent of flow stress, $\dot{\varepsilon}$ is the impact of the strain and $\frac{\dot{\varepsilon}}{\varepsilon_\circ}$ impact of strain rate. The Johnson cook parameters used for finite element modelling using explicit dynamics are presented, Table 3.

In this research work, the strain rate between the workpiece and tool contact during chip removal is defined by cumulative damage values during the modelling of the work material model. The constants are derived from the Split-Hopkinson pressure bar (SHPB) tests for plain carbon steel alloy [6, 28]. The expression for calculating the Johnson-Cook model of the damage constants is critical in analyzing flow stresses, Equation 8.

$$\varepsilon_{ef}^{p}=\left[d_1+d_1e^{\eta d_3}\right]\left[1+d_4ln\left(\frac{\dot{\varepsilon}^p}{\dot{\varepsilon}_{eo}^p}\right)\right]*\left[1-d_5\left(\frac{T-T_r}{T_m-T_r}\right)^m\right] \tag{8}$$

TABLE 3 Johnson-Cook parameters for AISI 1020 alloy [6, 30].

A [MPa]	B [MPa]	C	N	M	T_r (°C)	T_m (°C)
333	200	0.29	126	420	25	880

TABLE 4 Damage failure parameters for AISI 1020 alloy [30].

d_1	d_2	d_3	d_4	d_5	T_r (°C)	T_m (°C)
0.4313	5.93	8.42	−0.057	0	25	880

where: d_1-d_5 are failure damage parameters, temperatures, and strain rates. ε_{ef}^{p} is the strain rate reference, and η is the mean hydrostatic stress to the equivalent stress of the material, Table 4.

Temperature due to plastic deformation can be expressed under the adiabatic heating assumption, Equation 9.

$$\Delta T = \frac{\delta W^p}{\rho C_p} \tag{9}$$

where: ΔT is the difference between $T - T_r$, δ is the fraction of plastic work converted to heat, W^p is the plastic work done, ρ and C_p are the material density and the heat capacity, respectively.

2.4 | Friction modelling

Zorev's friction model is applied in modeling the mechanical contact between the tool and workpiece interface, Equation 10 [29].

$$\tau = \begin{cases} \tau_y, & \mu\sigma_n \geq \tau_y \\ \mu\sigma_n, & \mu\sigma_n < \tau_y \end{cases} \tag{10}$$

where: τ is the shear stress, τ_y is the shear yield strength, μ is Coulomb friction coefficient and σ_n is the normal stress on the tool rake face. Sliding and sticking are two distinct behaviors under Zorev's model. μ and σ_n were calibrated numerically as 0.4 (unit-less) and 350 MPa by comparing the measured and predicted chip thickness and residual stresses.

2.5 | Boundary conditions, element and mesh

Ansys software 2018 has been used to develop a finite element model in the orthogonal turning of AISI 1020 alloy because of its capability to capture minimum to maximum deformations, and high sensitivity to material non-linearity and strains.

The selected type of elements for the workpiece simulation is a nodal-based strain tetrahedral solid with bilinear type because of their high performance. The workpiece and the tool are meshed using a nodal-based strain element with 30000 nodal elements. The element size is automatically set to the default settings of the dynamic explicit environment while factoring in the size of the workpiece. The default size is 0.8 based on the design of experiments conducted to arrive at an optimal element size. The conditions for simulation of orthogonal cutting operation are based on the workpiece coordinate system,

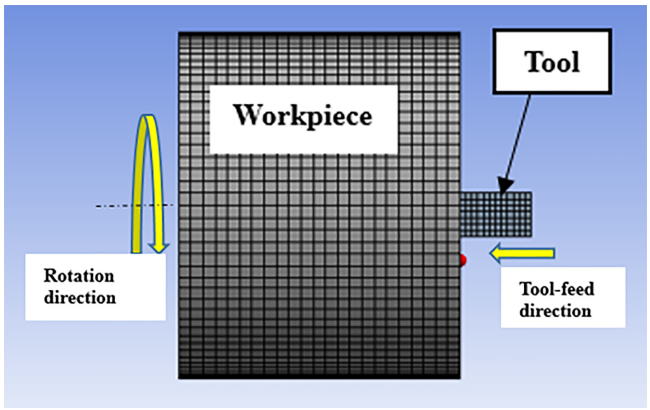

FIGURE 1 Boundary conditions for finite element model.

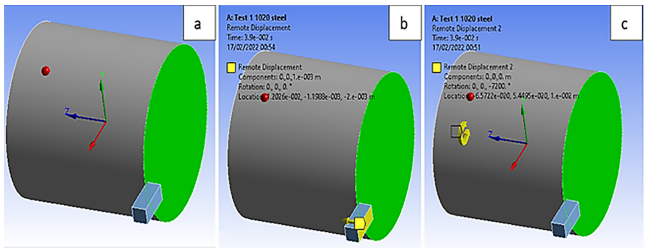

FIGURE 2 Boundary conditions for Rotation: a) Workpiece coordinate system b) Remote displacement 1, and c) Remote displacement 2.

TABLE 5 Design factors levels for simulation.

Factor	Level 1	Level 2	Level 3
Feed rate [mm/revolution]	0.2	0.4	0.6
Cutting speed [m/minute]	80	160	240
Depth of cut [mm]	0.2	0.4	0.6

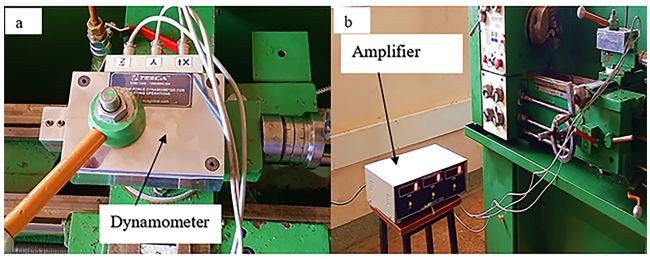

FIGURE 3 Experimental set-up for measurement of cutting forces: a) Dynamometer b) Amplifier.

TABLE 6 Induced residual stress measurement parameters and constants [30].

Work material	AISI 1020	Aperture	2 mm
Plane (hkl)	{211}	Working distance	39 mm
d-Spacing	0.117021 nm	X-ray irradiation time	30 s
Tube fluorescence	Cr–Kα	X-ray incidence angle	30°
Bragg angle	156.41°	Current	25 mA
Wavelength	0.2291	Voltage	30 kV

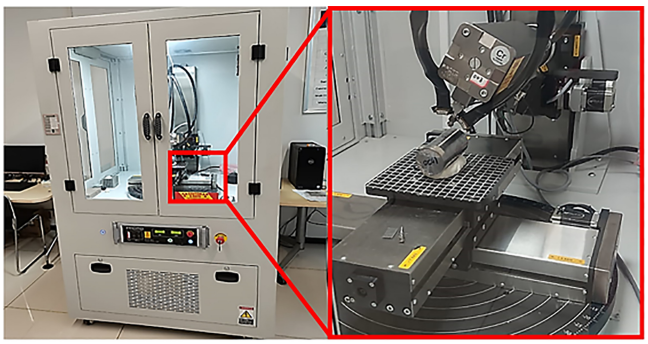

FIGURE 4 Proto-LXRD 1200 Stress mapping table with AISI 1020 alloy specimen.

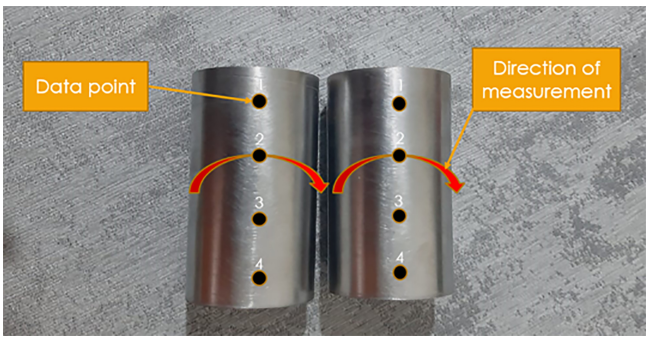

FIGURE 5 Data points and direction (circumferential) of residual stress measurement.

contact region between the workpiece and the cutting tool, and direction of workpiece and tool displacement, Figure 1.

The tool is modelled as a rigid body because of its high stiffness to the workpiece. A reference point must be assigned to the tool to capture the forces generated. The 3D finite element model setting for 3D orthogonal cutting simulation involves: Setting the boundary conditions, global coordinate system, workpiece coordinate system, tool-workpiece contact friction, target body, remote displacement 1 (provides direction and tool displacement), and displacement 2 (provides the angular rotation of the workpiece), Figure 2.

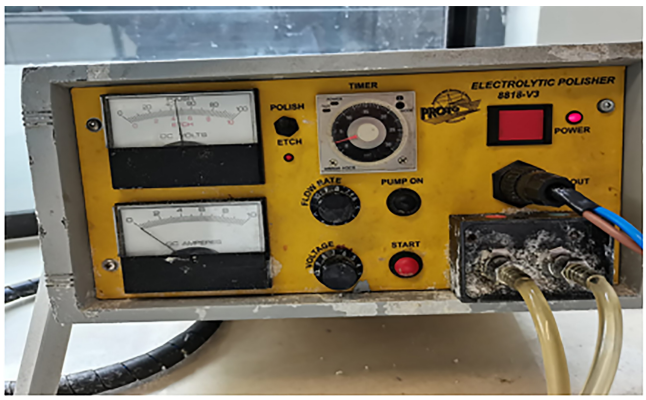

FIGURE 6 Proto electropolisher for removal of the surface layer.

2.6 | Finite element simulation-design of experiment

The present study uses the design of experiment using Minitab 18 software. The basic idea is to vary all relevant factors simultaneously over planned experiments and then connect the results through a mathematical model. This model is then used for interpretation and predictions. Three factors are considered in the investigation: cutting speed (v), feed rate (f), and depth of cut (d). The minimum and maximum levels are obtained from the design of the experiment performed on AISI 1020 alloy simulations, Table 5.

3 | EXPERIMENTAL TESTS FOR VALIDATION OF FINITE ELEMENT MODEL

The developed finite element model is validated by conducting force measurement using a tool dynamometer, residual stress measurement using an x-ray diffractometer, and measurement of chip thickness. The results are compared with the simulated results for verification and validation of the model.

FIGURE 7 Electropolishing the specimen in the circumferential direction.

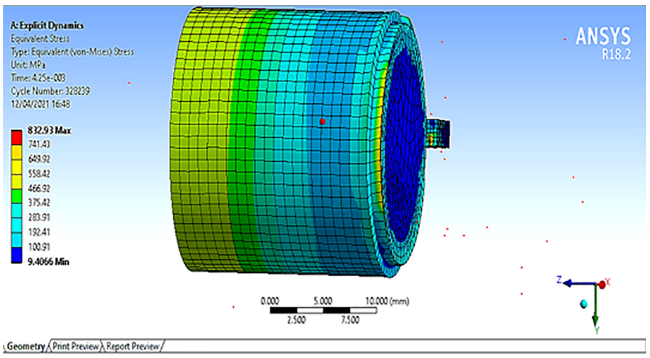

FIGURE 8 3D finite element model with a new cut surface (equivalent stress) for 360° turn.

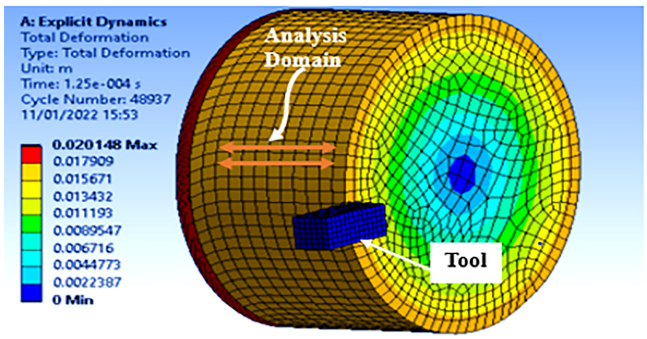

FIGURE 9 Deformation nephogram (meshed) after unloading cutting tool and cooling of the workpiece.

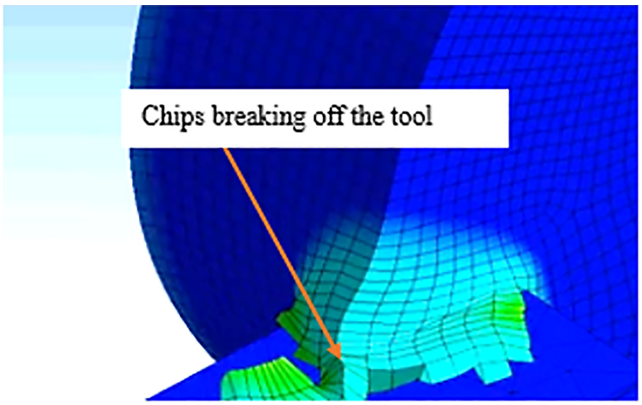

FIGURE 10 Chip formation in simulated orthogonal cutting at a speed of 240 m/minute, feed rate 0.4 mm/revolution, and depth of cut 0.6 mm.

3.1 | Measurement of forces

Turning tests are conducted on Chester Bristol variable speed lathe machine (Chester, Wales) and using the high-speed steel T1 cutting tool. The work material was AISI 1020 alloy- solid shafts cut into 27 pieces, each with 45 mm diameter and 200 mm length. During the orthogonal operation, cutting force components (x, y, and z) were measured using a Kistler (type 9127) 3-component piezoelectric dynamometer (Kistler, United States), amplified using the type 5167A oscilloscope (Kistler, United States) and results were treated by Dynoware software, Figure 3.

Three components of forces in three directions, x, y, and z are obtained from the amplifier and results are recorded. The resultant cutting force is calculated as represented by Equation 11

$$F = \sqrt{(F_x^2 + F_y^2 + F_z^2)} \tag{11}$$

where: F is the resultant cutting force F_x^2 is the primary cutting force (tangential), F_y^2 and F_z^2 are feed force and radial force, respectively. In the calculation of the resultant cutting forces, the feed (the third component) force (F_y^2) from the dynamometer is ignored. The values of (F_y^2) are of negligible magnitude.

3.2 | Residual stress measurement

The residual stresses are measured based on the x-ray diffraction method using a Proto-LXRD 1200 x-ray stress analyzer machine (Proto Manufacturing, United States) fitted with a modular stress mapping system and Proto Software for analyzing residual stress using the $Sin^2\Psi$ method, Figure 4.

The Proto -LXRD 1200 stress analyzer has 9 β angles with a maximum of 30°. X-ray diffraction constants and

TABLE 7 Simulation and experiment resultant cutting forces.

Run order	Speed v [m/minute]	Feedrate f [mm/revolution]	Depth of cut, d [mm]	Simulation force, F [N]	Experiment force, F [N]	Error margin	% Error
1	80	0.2	0.2	330.2	334.1	3.9	1.17
2	80	0.2	0.4	343.1	337.3	−5.8	−1.72
3	80	0.2	0.6	345.2	341.5	−3.7	−1.08
4	80	0.4	0.2	358.1	361.3	3.2	0.89
5	80	0.4	0.4	345.1	348.7	3.6	1.03
6	80	0.4	0.6	360.3	361.9	1.6	0.44
7	80	0.6	0.2	365.3	363.8	−1.5	−0.41
8	80	0.6	0.4	370.5	364.7	−5.8	−1.59
9	80	0.6	0.6	380.2	375.8	−4.4	−1.17
10	160	0.2	0.2	420.1	417.9	−2.2	−0.53
11	160	0.2	0.4	487.3	483.8	−3.5	−0.72
12	160	0.2	0.6	478.4	474.5	−3.9	−0.82
13	160	0.4	0.2	456.4	463.2	6.8	1.47
14	160	0.4	0.4	425.2	428.3	3.1	0.72
15	160	0.4	0.6	430.5	433.8	3.3	0.76
16	160	0.6	0.2	445.1	441.2	−3.9	−0.88
17	160	0.6	0.4	430.2	434.6	4.4	1.01
18	160	0.6	0.6	445.8	451.2	5.4	1.20
19	240	0.2	0.2	545.4	551.7	6.3	1.14
20	240	0.2	0.4	578.6	574.1	−4.5	−0.78
21	240	0.2	0.6	575.2	579.3	4.1	0.71
22	240	0.4	0.2	574.2	569.8	−4.4	−0.77
23	240	0.4	0.4	587.6	583.5	−4.1	−0.70
24	240	0.4	0.6	554.2	560.6	6.4	1.14
25	240	0.6	0.2	554.6	552.4	−2.2	−0.40
26	240	0.6	0.4	540.4	546.3	5.9	1.08
27	240	0.6	0.6	530.7	527.9	−2.8	−0.53

TABLE 8 The average chip thickness from selected runs.

Case study	Simulated chip thickness [mm]	Experiment chip thickness [mm]	% Error
Run 2	0.168	0.163	3.07
Run 4	0.166	0.164	1.22
Run 7	0.171	0.169	1.18
Run 11	0.194	0.183	6.01
Run 12	0.198	0.193	2.59
Run 17	0.208	0.204	1.96
Run 23	0.212	0.207	2.42
Run 24	0.214	0.212	0.94
Run 27	0.218	0.214	1.86

parameters for induced residual measurement are obtained from the American Society for Testing and Materials E915-2019, Table 6 [30].

The induced residual stress is measured in the circumferential direction at four labeled points, and the average results are recorded, Figure 5.

The sample for in-depth residual stress is turned at a speed of 160 m/minute, feed rate (0.6 mm/revolution), and depth of cut 0.6 mm. The analysis of induced residual stress below the superficial layer is conducted by removing successful layers using a proto electropolishing model 8818-V3 (Proto Manufacturing, United States) machine, Figure 6.

The direct current supply's positive (+) terminal is connected to the anode and the negative (−) terminal to

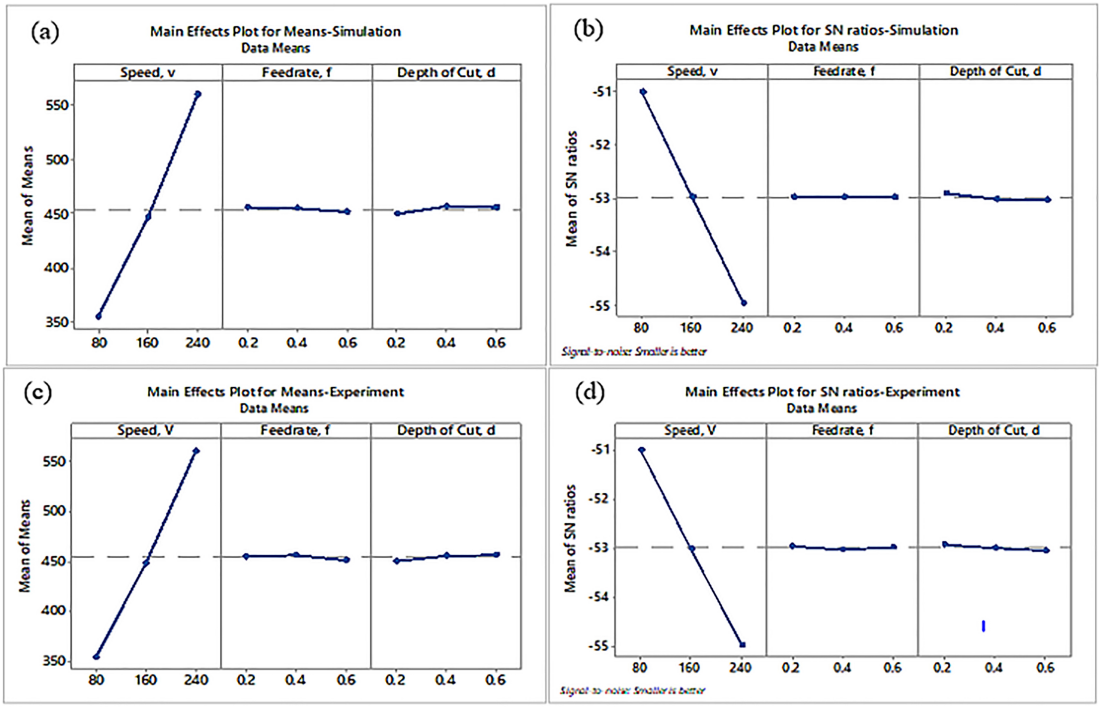

FIGURE 11 Response for means and signal to noise ratio (S/N) for resultant cutting forces: (a) and (b) simulation plots (c) and (d) experiment plots.

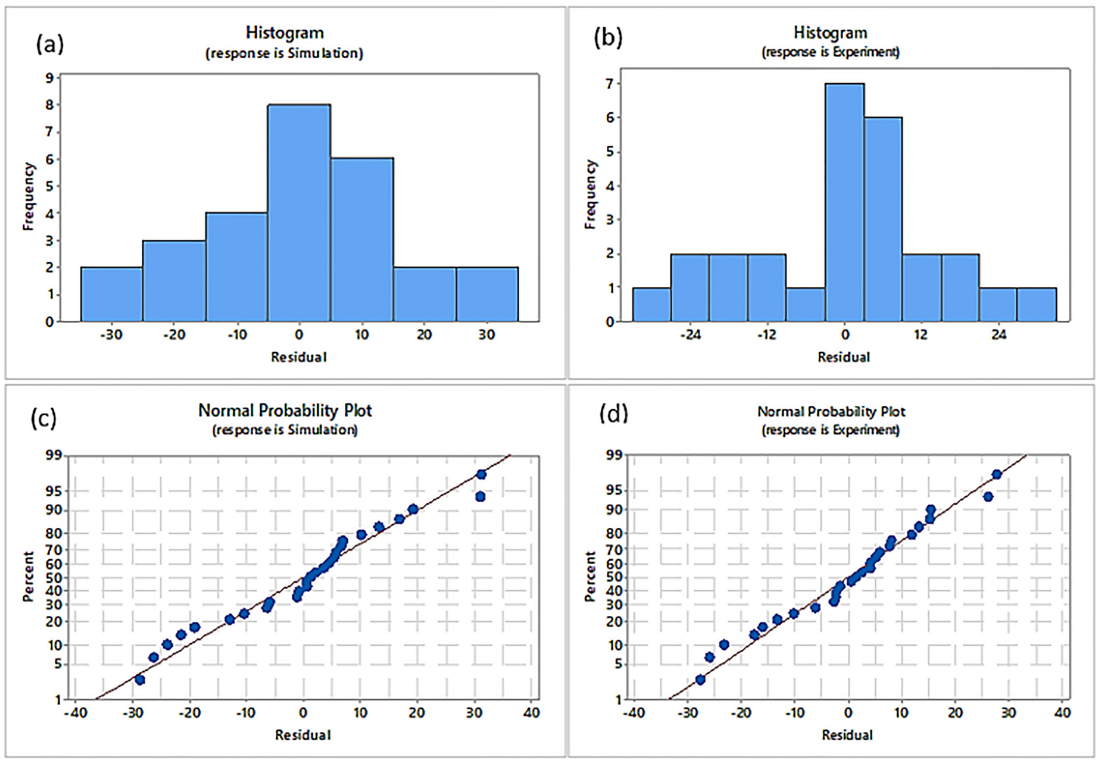

FIGURE 12 Comparison of residual histograms (a, b) and normal probability plots (c, d) for simulation and experiment.

TABLE 9 General linear model-analysis of variance results for simulation.

Source	Degree of freedom	Sum squares	Mean squares	F-value	P-value	Contribution %
Speed, v	2	189430	94714.8	448.84	0.000	95.23
Feedrate, f	2	97	48.7	0.23	0.799	0.05
Depth of cut, d	2	226	113.0	0.54	0.605	0.11
Speed * feedrate	4	4105	1026.4	4.86	0.028	2.06
Speed * depth of cut	4	539	134.6	0.64	0.650	0.27
Feedrate * depth of cut	4	2827	706.8	3.35	0.068	1.42
Error	8	1688	211.0			0.85
Total	26	198912				100

TABLE 10 General linear model-analysis of variance results for experiment.

Source	Degree of freedom	Sum squares	Mean squares	F-value	P-value	Contribution %
Speed, v	2	192062	96031.1	383.05	0.000	95.92
Feedrate, f	2	164	82.1	0.33	0.730	0.08
Depth of cut, d	2	176	87.9	0.35	0.715	0.09
Speed * feedrate	4	3365	841.2	3.36	0.068	1.68
Speed * depth of cut	4	454	113.5	0.45	0.768	0.23
Feedrate * depth of cut	4	2002	500.5	2.00	0.188	0.99
Error	8	2006	250.7			1.00
Total	26	200228				100

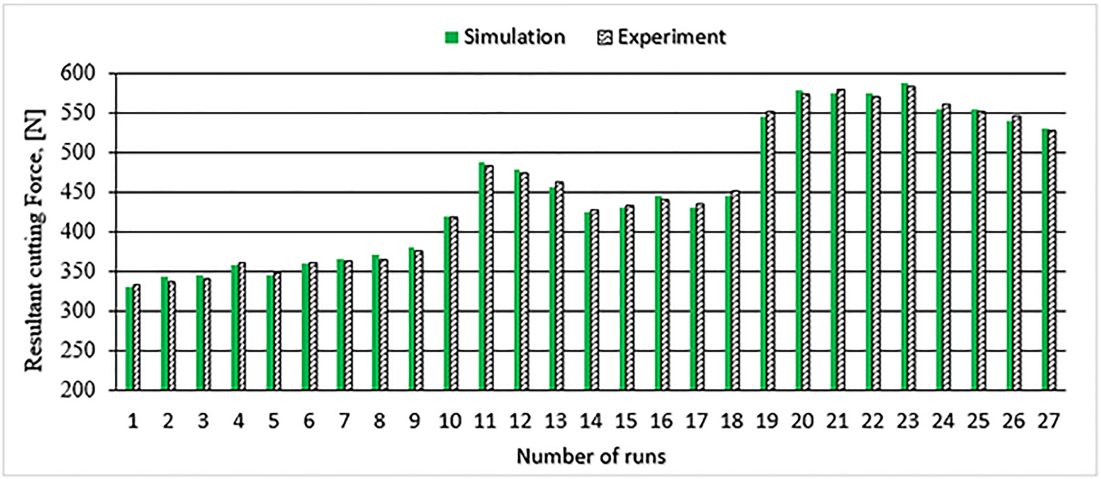

FIGURE 13 Experimental and simulation resultant cutting forces for 27 runs.

the cathode. The AISI 1020 alloy cylindrical specimen acts as the cathode. A 45 kV voltage was applied for a set of times depending on the removal depth. The depth must be preset and current variation per time to yield the depth required, Figure 7.

To ensure the finish's quality, the new layer's surface roughness was measured using a Mitutoyo SJ-400 profilometer (Mitutoyo, Kawasaki). The induced residual stress along the depth is measured at 20 μm, 40 μm, and 60 μm from the surface of the specimen. After removing

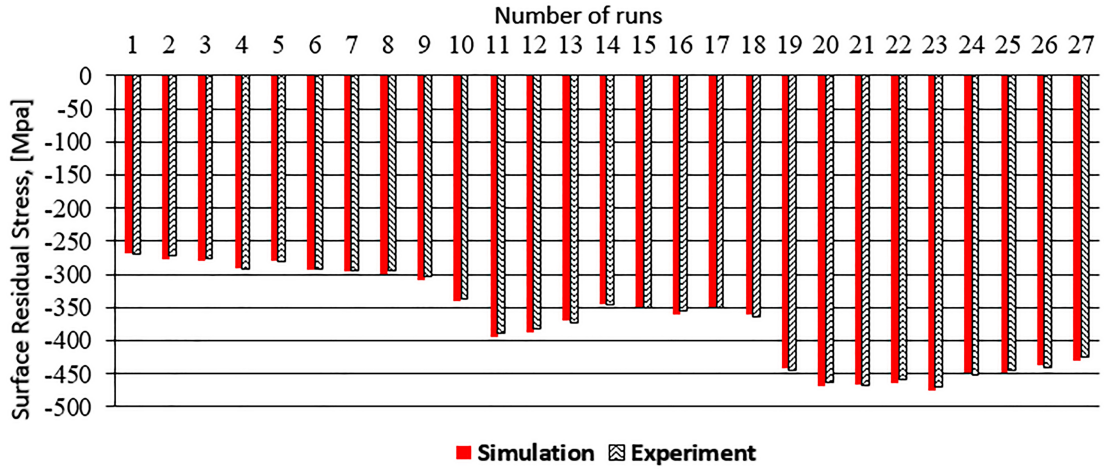

FIGURE 14 Comparison between experiment and simulation surface residual stress.

TABLE 11 Simulation and experiment superficial residual stress.

Run No.	Speed, v [mm/min]	Feedrate, *f* [mm/revolution]	Depth of cut, d [mm]	Simulated residual stress [MPa]	Experiment residual stress [MPa]	Error margin	% Error
1	80	0.2	0.2	−267.5	−269.0	1.5	0.55
2	80	0.2	0.4	−277.9	−271.5	−6.4	2.35
3	80	0.2	0.6	−279.6	−274.9	−4.7	1.71
4	80	0.4	0.2	−290.1	−290.8	0.8	0.27
5	80	0.4	0.4	−279.5	−280.7	1.2	0.42
6	80	0.4	0.6	−291.8	−291.3	−0.5	0.18
7	80	0.6	0.2	−295.9	−292.9	−3.0	1.04
8	80	0.6	0.4	−300.1	−293.6	−6.5	2.22
9	80	0.6	0.6	−308.0	−302.5	−5.4	1.80
10	160	0.2	0.2	−340.3	−336.4	−3.9	1.15
11	160	0.2	0.4	−394.7	−389.5	−5.3	1.35
12	160	0.2	0.6	−387.5	−382.0	−5.5	1.45
13	160	0.4	0.2	−369.7	−372.9	3.2	0.86
14	160	0.4	0.4	−344.4	−344.8	0.4	0.11
15	160	0.4	0.6	−348.7	−349.2	0.5	0.14
16	160	0.6	0.2	−360.5	−355.2	−5.4	1.51
17	160	0.6	0.4	−348.5	−349.9	1.4	0.40
18	160	0.6	0.6	−361.1	−363.2	2.1	0.58
19	240	0.2	0.2	−441.8	−444.1	2.3	0.53
20	240	0.2	0.4	−468.7	−462.2	−6.5	1.41
21	240	0.2	0.6	−465.9	−466.3	0.4	0.09
22	240	0.4	0.2	−465.1	−458.7	−6.4	1.40
23	240	0.4	0.4	−476.0	−469.7	−6.2	1.33
24	240	0.4	0.6	−448.9	−451.3	2.4	0.53
25	240	0.6	0.2	−449.2	−444.7	−4.5	1.02
26	240	0.6	0.4	−437.7	−439.8	2.0	0.47
27	240	0.6	0.6	−430.0	−425.0	−5.1	1.19

TABLE 12 **F** Means response for a signal to noise ratio-simulation tests.

Level	Speed [m/min]	Feedrate [mm/revolution]	Depth of cut [mm]
1	−49.17	−51.15	−51.07
2	−51.16	−51.15	−51.18
3	−53.13	−51.16	−51.21
Delta	3.96	0.01	0.13
Rank	1	3	2

TABLE 13 Means response for signal to noise ratio-experimental tests.

Level	Speed [m/minute]	Feedrate [mm/revolution]	Depth of cut [mm]
1	−49.11	−51.05	−50.99
2	−51.12	−51.14	−51.13
3	−52.99	−51.03	−51.11
Delta	3.88	0.11	0.14
Rank	1	3	2

each successful layer, a new measurement on the x-ray diffractometer is conducted to pick the new data at each point and the average results recorded.

4 | RESULTS AND DISCUSSION

4.1 | Resultant cutting forces results

The resultant cutting forces from the finite element model simulation and the experiment indicate an agreement. The percentage error of less than 2% is realized when resultant cutting forces are compared between the simulation and experimental results. However, it is noted that with an increase in the range of cutting speed, feed rate, and depth of cut, the cutting forces in both cases increase significantly to values of 587 N for the experiment and 583 N for Simulation results, Table 7.

An increase in cutting speed, feed rate, and depth of cut leads to tool deflection, rising temperature affecting the tool's cutting edge, and hence more cutting energy in the surface region is required to remove the chips, leading to the increase in resultant cutting forces.

TABLE 14 Analysis of variance for stimulation-induced residual stress.

Source	Degree of freedom	Sum squares	Mean squares	F-value	P-value	Contribution %
Speed, v	2	124313	62156.3	449.32	0.000	95.23
Feedrate, f	2	63	31.6	0.23	0.801	0.048
Depth of cut, d	2	149	74.3	0.54	0.604	0.11
Speed * feedrate	4	2689	672.4	4.86	0.028	2.06
Speed * depth of cut	4	351	87.8	0.63	0.652	0.29
Feedrate * depth of cut	4	1855	463.7	3.35	0.068	1.42
Error	8	1107	138.3			0.85
Total	26	130527				100

TABLE 15 Analysis of variance for experiment-induced residual stress.

Source	Degree of freedom	Sum squares	Mean square	F-value	P-value	Contribution %
Speed, v	2	116470	58235.0	412.61	0.000	94.76
Feedrate, f	2	243	121.4	0.86	0.459	0.20
Depth of cut, d	2	197	98.3	0.70	0.526	0.16
Speed * feedrate	4	2578	644.4	4.57	0.033	2.08
Speed * depth of cut	4	516	129.0	0.91	0.500	0.42
Feedrate * depth of cut	4	1776	444.0	3.15	0.079	1.45
Error	8	1129	141.1			0.92
Total	26	122908				100

4.2 | Chip thickness

As part of the validation of the finite element model, chip thickness was measured using a digital micrometer, and experiment results were compared with the simulation ones. The predicted chip thickness compared with experimental results was obtained and recorded. The experimental values were measured using the ultrasonic thickness gauge model UM-3 (Xiuyan, Yahe), with a measuring resolution of 0.001 mm. The comparison results showed less than 6.01% variation, hence verifying the finite element model developed using Ansys explicit dynamics. The case studies were randomly selected to analyze the chip thickness, Table 8.

The simulation nephogram of the newly generated surface at a cutting speed of 80 m/minute, feedrate 0.2 mm/revolution, was suitable in chip generation at a depth of cut 0.2 mm (run 1) at maximum equivalent (Von-Mises) stress of 741.43 MPa for one revolution, Figure 8.

The workpiece rotates 360° while the cutting tool advances by cutting a depth of 0.2 mm along the length of the workpiece. The average time for a single simulation was 3 hours. The computer specifications for simulation and modelling were core i7 with a RAM of 16 GB and 1 TB hard disk space. The residual stresses were extracted from the newly cut surface on explicit dynamics and results were automatically recorded. After unloading the cutting tool and cooling the workpiece at a cutting speed of 160 m/minute, feedrate 0.4 mm/revolution, and depth of cut 0.4 mm for 20 mm, the meshed simulation nephogram with meshes are obtained, with maximum deformation of 0.0020148, Figure 9.

TABLE 16 Residual stress beneath the surface.

Depth beneath surface [μm]	Induced residual stress, [MPa]		% Error
	Simulation	Experiment	
0	−311	−320	2.81
20	−255	−260	1.92
40	−235	−233	0.86
60	−222	−211	5.21

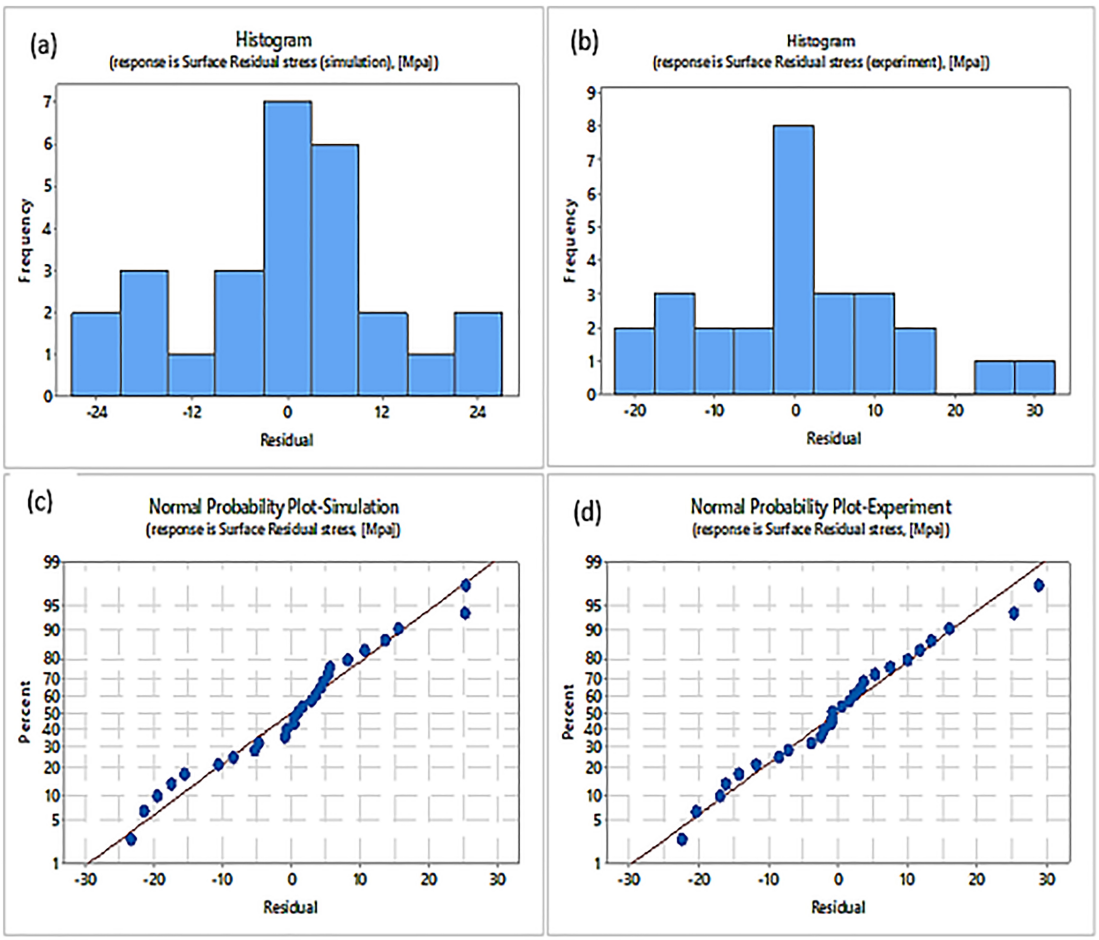

FIGURE 15 Comparison of residual histograms (a, b) and normal probability plots (c, d) for surface residual stresses.

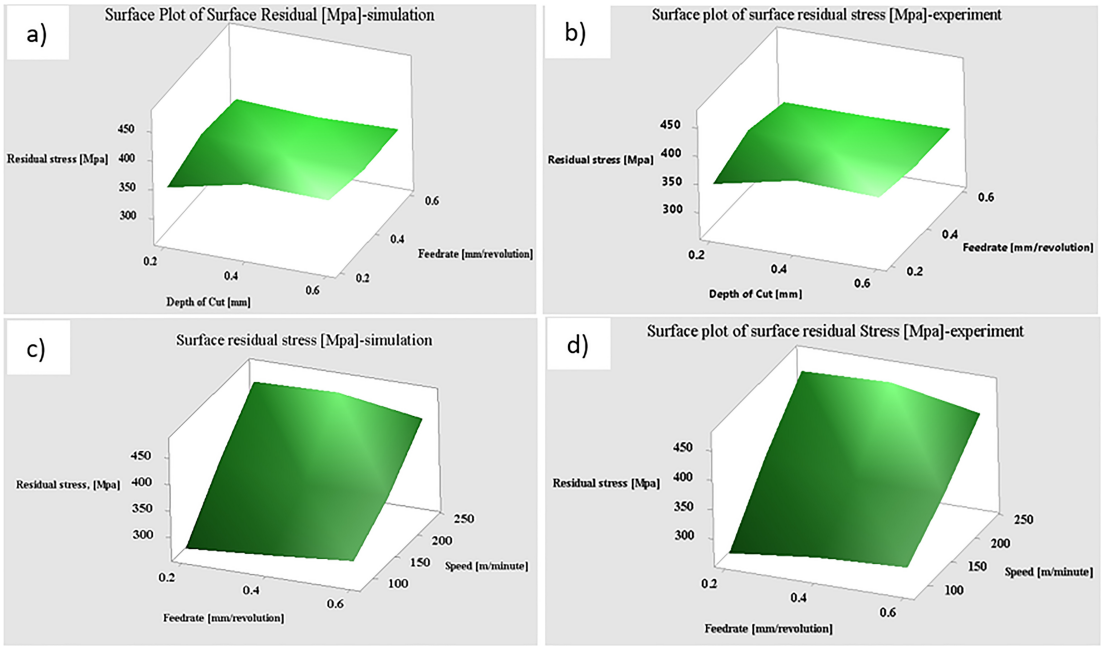

FIGURE 16 Surface plots: Depth of cut versus feed rate (a) simulation, (b) experiment. Feed rate versus speed (c) simulation (d) experiment.

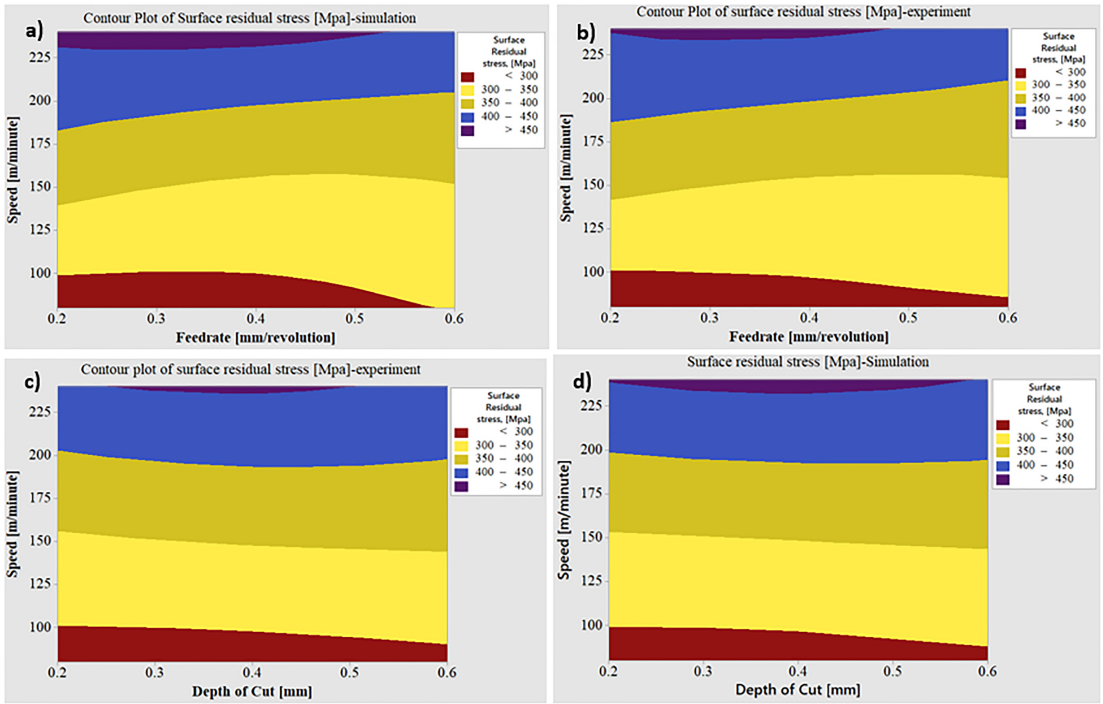

FIGURE 17 Contour plot for surface residual stress (a) Cutting speed versus feed rate (simulation), (b) Cutting speed versus feed rate (experiment), (c) Cutting speed versus depth of cut (experiment), (d) Cutting speed versus depth of cut (simulation).

Depending on the combined variables, continuous and discontinuous chips were formed during the orthogonal simulation. The interaction between the tool's cutting edge and workpiece leads to an increase in thermal temperatures; hence, the depth of cut determines the sizes of chips. It was observed that thick layers of discontinuous chips formed with an increase in depth of cut as demonstrated, Figure 10.

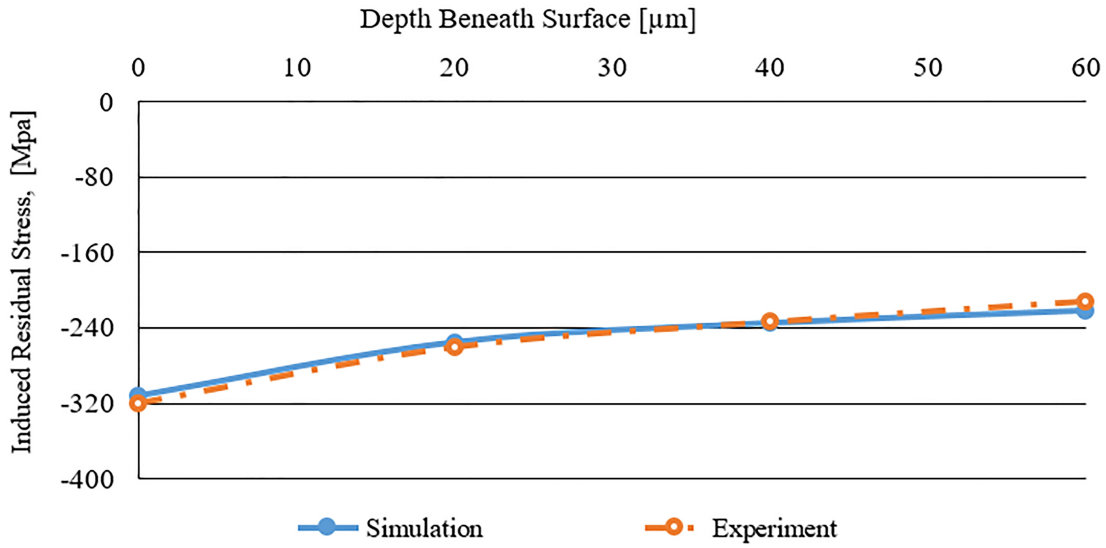

FIGURE 18 Induced residual stress on varying depths from the surface.

4.3 | Analysis of data using Taguchi's method

Taguchi uses a loss function to find the difference between the experimental and target values, which is again converted into the signal-to-noise ratio (SNR), the ratio of mean to standard deviation [21]. In the present study, the signal-to-noise ratio for the smaller, the better is adopted for resultant cutting forces as a response, Equation 12.

$$SNR = -10\ log\frac{1}{n}\sum R^2 \tag{12}$$

Taguchi analysis was done using Minitab 18 software tool and the means plot, signal-to-noise ratio plots and analysis of variance results were obtained and presented. Based on the data response from simulation, main effect plots for data means show the response of the optimum levels for cutting speed, feed rate, and depth of cut, Figure 11a, c. The cutting speed is ranked first as the most influential, followed by the depth of cut and the feed rate in both simulation and experimental resultant forces, Figure 11b, d.

The response for means and Signal to Noise ratio for both simulation and experiment show a close correlation (0.998) therefore validating the finite element model for cutting forces. Also, on comparing histograms for residuals versus the frequency for the resultant cutting forces, the histograms show a normal distribution trend with the highest frequencies of 8 for simulation versus 7 for the experiment, Figure 12a, b. The normal probability plots indicate normal distribution; hence data near the mean are more frequent in both simulation and experiment, Figure 12b, c.

The finite element model was accurate because of the minimal variance when a comparison is drawn between experimental and simulation results are compared.

Performing regression analysis for the resultant cutting forces, cutting speed (v), feed rate (f), and depth of cut (d), parameters produced model equations. The regression model equation from simulation and experimental results had a correlation value of 96% to 97%. The model equations had a p-value of $\ll 0.05$ hence statistically significant, Equation 13–14.

$$\begin{aligned} F(simulation) = {} & 454.00 - 98.66v - 7.44v + \\ & 106.10v + 1.95f + 0.63f - 2.57f - 4.06d + 2.45d + \\ & 1.61d - 17.78v^*f - 1.46v^*f + 19.24v^*f + 13.43v^*f - \\ & 9.81v^*f - 3.61v^*f + 4.35v^*f + 11.27v^*f - \\ & 15.63v^*f - 0.07v^*d - 4.88v^*d + 4.95v^*d - 1.96v^*d - \\ & 1.44v^*d + 3.40v^*d + 2.03v^*d + 6.32v^*d - \\ & 8.35v^*d - 19.8f^*d + 11.27f^*d + 8.71f^*d + \\ & 12.34f^*d - 4.44f^*d - 7.90f^*d + 7.64f^*d - \\ & 6.84f^*d - 0.80f^*d \end{aligned} \tag{13}$$

$$F(experiment) = 454.19 - 99.85v - 6.58v + 106.43v + 0.72f + 2.60f - 3.31f - 3.59d + 1.51d + 2.09d - 17.43v^*f + 0.36v^*f + 17.07v^*f + 10.40\ v^*f - 8.44\ v^*f - 1.96\ v^*f + 7.03\ v^*f + 8.08\ v^*f - 15.11\ v^*f + 2.31\ v^*d - 5.62\ v^*d + 3.30\ v^*d - 3.25\ v^*d - 0.22\ v^*d + 3.47\ v^*d + 0.94\ v^*d + 5.84\ v^*d - 6.77\ v^*d - 16.75\ f^*d + 8.65\ f^*d + 8.10\ f^*d + 11.57\ f^*d - 4.80\ f^*d - 6.77\ f^*d + 5.18\ f^*d - 3.85\ f^*d - 1.33\ f^*d \quad (14)$$

From the simulation of resultant cutting forces, cutting speed had a more significant contribution (95.23%), followed by feed rate (0.05%). For combined parameters, the cutting speed and feed rate showed a contribution of 0.11%. The regression model equations were statistically significant because their coefficients had a probability value < 0.05, Table 9.

The experimental results for cutting forces also confirm that cutting speed contributed 95.92%, followed by the depth of cut (0.09%). The influence of combined factors shows cutting speed-feed rate leading with a contribution of 2.06%. From the model, the selected parameters and their combination form a regression model equation for minimization of varied resultant cutting forces during orthogonal cutting of AISI 1020 alloy, Table 10.

The resultant cutting forces were compared against the 27 runs. On each run, cutting conditions, and parameters, the results showed a close range of resultant cutting forces in simulation and experiment. There is a significant increase in resultant cutting forces for cutting speed of 160 m/minute, feed rate (0.4 mm/revolution to 0.6 mm/revolution), and depth range of 0.4 mm to 0.6 mm, Figure 13.

4.4 | Superficial residual stresses

The measured and simulated data for residual surface stress was obtained for the 27 runs. The percentage error between the simulated and measured superficial residual stress was between 0.09% and 2.35%, Table 11.

The deviation between experiment and simulation values can be attributed to the selected boundary conditions during the experiment. The average superficial stress for 27 runs from simulation and the experiments are 367.7 MPa and 365.6 MPa, respectively. The plots of surface residual stress versus the number of runs showed close-range values with minimal margin errors for each specific simulation and experimental test, Figure 14.

4.5 | Analysis of data using Taguchi's method

The plot shows that among the main effects, the cutting speed and depth of cut were the most important factors influencing the magnitude of the induced residual on AISI 1020 alloy during the turning operation, Tables 12, 13.

The analysis of variance indicated cutting speed had a contribution of 95.23%, feed rate 0.048%, and depth of cut 0.11% in the formation of residual stress during simulation, a consistent indication compared to experimental results analysis, Table 14.

The analysis of variance indicated cutting speed had a contribution of 94.76%, feed rate 0.20%, and depth of cut 0.16% in the formation of residual stress for experimental results. In both cases, variation of the speed enhanced residual stress formation on sub-surface layers of the AISI 1020 alloy, Table 15.

4.6 | The induced residual stress model

Predictive model equations were derived from regression analysis to establish a relationship between input variables; cutting speed (v), feed rate (f), depth of cut (d), and response (induced residual stress), both for simulation and experimental results, Equation 15–16.

Simulation:

$$Residual\ stress,\ [Mpa] = 112.3 + 1.403v + 181.2f + 117.7d - 0.721v^*f - 0.194v^*d - 188f^*d \quad (15)$$

Experiment:

$$Residual\ stress,\ [Mpa] = 120.8 + 1.382v + 164.1f + 100.2d - 0.742v^*f - 0.201v^*d - 145f^*d \quad (16)$$

The results showed that cutting speed had a significant effect since the probability value for cutting speed was < 0.005. However, the interaction between input variables had no contribution since their p values were > 0.005, Tables 15, 16. Both regression model equations are presented, and both had probability values of 0.000 hence significant.

The correlation coefficient was very close to unity (0.999) from the results of both the resultant cutting forces and the induced residual stresses for the AISI 1020 alloy.

The histogram residuals between simulation and experiment showed normal distribution with insignificant

variance, Figure 15a, b. The comparison of normal probability plots for finite element model versus cutting parameters (simulation and experiment) showed uniformity, hence negligible variation, confirming the model's accuracy, Figure 15c, d.

The effects of feed rate and depth of cut were compared and conducted by constructing 3-dimensional surface plots. The plots showed a steady increase of induced residual stress with a sharp increase in feed rate and depth of cut, Figure 16a, b. However, a sharp increase in surface residual stress occurred when the cutting speed was compared with feed rate, depicting the higher contribution of cutting speed during surface residual stress induction, Figure 16c, d.

The two-dimensional contour plots were plotted to understand the contribution of the individual parameters. Cutting speed contributed significantly to induced surface residual stress with rising feed rate influence, Figure 17a, b. A contour plot of cutting speed versus depth of cut again showed the cutting speed as the most influencing parameter in residual stress formation while the depth of cut had a minimal contribution, Figure 17c, d.

4.7 | Induced residual stress beneath surface

An experiment for measuring induced residual stress beneath the surface was conducted, and the results were obtained for various depths, Table 14. Based on the development, the percentage error between the simulation and experiment was less than 5.21% hence verifying the accuracy of the finite element model. The simulation and experimental results were compared and presented, Table 16.

The graphical comparison of induced residual stress and beneath depth shows close agreement between experiment and simulation values. The induced residual stresses were compressive and showed a steady decrease between depths of 40 μm and 60 μm, Figure 18.

5 | CONCLUSIONS

This research work aimed to model and simulate the machining of induced residual stresses using the finite element method. The influence of cutting speed, feed rate, and depth of cut was determined through this. It is concluded that:

1. The cutting speed had the highest contribution in inducing external residual stress on turned cylindrical shafts. From the simulation results, the cutting speed contributed 95.24%, while it had 94.76% from experimental results. The interactions between input parameters were statistically insignificant (probability value >0.005).
2. In the analysis of variance for resultant cutting forces, the cutting speed had the highest contribution of 95.23%, as compared to the depth of cut, which had 0.11%. The feed rate had the lowest contribution of 0.05%.
3. The correlation coefficient was close to unity for predictive model equations for both resultant forces and induced residual stresses. They were statistically significant with a probability value of <0.005.
4. In comparison between the simulation and experimental results, the margin of error for resultant cutting forces was $<2\%$ and for in-depth residual stress $<6\%$. The variability of measured and simulated results was in good agreement, verifying the finite element model.

REFERENCES

1. J. Outeiro, *CIRP Encycl. Prod. Eng* **2019**, 1440.
2. A. R. C. Sharman, J. I. Hughes, K. Ridgway, *J. Mater. Process. Technol.* **2005**, *173*, 359.
3. D. Yang, X. Xiao, X. Liang, *Int. J. Adv. Manuf.* **2019**, *5*, 2965.
4. F. Wöste, J. Kimm, J. A. Bergmann, W. Theisen, P. Wiederkehr, *Prod. Eng.* **2021**, *15*, 873.
5. W. Jomaa, V. Songmene, P. Bocher, *Materials (Basel).* **2014**, *7*, 1603.
6. M. Bashistakumar, B. Pushkal, *J. Eng. Sci.* **2018**, *5*, A1.
7. A. K. Mishra, P. Shandilya, Presented at *AIMTDR*, Guwahati, Assam, India on December 12 -December 14, **2014**, 1–6.
8. C. Shan, M. Zhang, S. Zhang, J. Dang, *Int. J. Adv. Manuf. Technol.* **2020**, *107*, 2375.
9. S. Sai Venkatesh, T. A. Ram Kumar, A. P. Blalakumhren, M. Saimurugan, K. Prakash Marimuthu, *Mech. Mech. Eng.* **2019**, *23*, 297.
10. U. Silva, C. Diniz, S. Rocha, J. Filho, R. Pereira, A. Filho, P. Maia. Presented at *SAEBID*, Sao Paulo, Brasil on September 22-September 24, **2015**, 8.
11. P. Krishnakumar, K. Prakash Marimuthu, K. Rameshkumar, K. I. Ramachandran, *Int. J. Mach. Mach. Mater.* **2013**. *14*, 213.
12. V. G. Navas, O. Gonzalo, I. Bengoetxea, *Int. J. Mach. Tools Manuf.* **2012**, *61*, 48.
13. A. Molinari, A. Moufki, *Int. J. Mech. Sci.* **2008**, *50*, 124.
14. K. Jacobus, R. E. DeVor, S. G. Kapoor, *J. Manuf. Sci. Eng. Trans.* **2000**, *122*, 20.
15. S. S. Sarnobat, H. K. Raval, *Meas. J. Int. Meas. Confed.* **2019**, *131*, 235.
16. H. A. Soliman, A. Y. Shash, T. M. El-Hossainy, M. Abd-Rabou, *Eng. Rep.* **2020**. *2*, e12240.

17. M. Javidikia, M. Sadeghifar, V. Songmene, M. Jahazi, *Int. J. Adv. Manuf. Technol.* **2020**, *106*, 4547.
18. H. J. Hu, W. J. Huang, *Int. J. Adv. Manuf. Technol.* **2013**, *67*, 907.
19. Z. Qi, B. Li, L. Xiong, *Front. Mech. Eng.* **2014**, *9*, 265.
20. M. Sadeghifar, R. Sedaghati, W. Jomaa, V. Songmene, *Int. J. Adv. Manuf. Technol.* **2018**, *96*, 3747.
21. B. V. Ramnath, S. Sharavanan, J. Ismail, S. B. Mohamed, S. Yalcinkaya, *Iop. Conf. Ser. Mater. Sci. Eng.* **2017**, *225*, 012186.
22. T. D. Marusich, S. Usui, R. J. McDaniel, *Int. Mech. Eng. Congress Expo.* **2003**, *37203*, 95.
23. B. Haddag, S. Atlati, M. Nouari, M. Zenasni, *Heat Mass Transf. und Stoffuebertragung* **2015**, *51*, 1355.
24. D. Boing, R. B. Schroeter, A. J. de Oliveira, *Wear* **2018**, *398*, 69.
25. R. T. Coelho, E. G. Ng, M. A. Elbestawi, *Int. J. Mach. Tools Manuf.* **2007**, *47*, 263.
26. L. Tu, W. Shi, *Metals (Basel).* **2020**. *10*, 33.
27. M. Mahnama, M. R. Movahhedy, *J. Manuf. Process.* **2012**, *14*, 188.
28. A. Banerjee, S. Dhar, S. Acharyya, D. Datta, N. Nayak, *Mater. Sci. Eng. A* **2015**, *640*, 200.
29. C. R. Liu, Y. B. Guo, *Int. J. Mech. Sci.* **2000**, *42*, 1069.
30. ASTM Int. *ASTM E. 915–19*, **2019**.

How to cite this article: R. N. Bosire, O. M. Muvengei, J. M. Mutua, J. K. Kimotho, *Materialwiss. Werkstofftech.* **2023**, *54*, e202200088. https://doi.org/10.1002/mawe.202200088